Liu et al. *Zool. Res.* 2026, 47(3): 811−826
https://doi.org/10.24272/j.issn.2095-8137.2025.141
https://cstr.cn/32248.14.zr.2025.141

ZR | Zoological Research

Article Open Access

# Gut microbiota remodeling in *HBB*-mutant cynomolgus monkeys reveals blood-gut axis disruption associated with β-thalassemia-related gastrointestinal dysfunction

Bao-Zhen Liu[1,2,3,#], Xin-Yuan Zhao[2,#], Ze-Wen Sun[4,#], Jun Wang[1,6], Jing-Tao Zeng[2], Yan Huang[2], Ke-Qi Cai[5], Jian-Guo Zhao[3,4], Shi-Hua Yang[2,*], Jing-Li Yuan[1,2,3,*]

[1] *Innovation Center of Academician Xia Xianzhu's Team*, *Key Laboratory of Tropical Animal Breeding and Disease Research*, *Institute of Animal Science and Veterinary Medicine*, *Hainan Academy of Agricultural Sciences*, *Haikou*, *Hainan* 571100, *China*
[2] *College of Veterinary Medicine*, *South China Agricultural University*, *Guangzhou*, *Guangdong* 510642, *China*
[3] *Sanya Institute*, *Hainan Academy of Agricultural Sciences*, *Sanya*, *Hainan* 572019, *China*
[4] *State Key Laboratory of Stem Cell and Reproductive Biology*, *Institute of Zoology*, *Stem Cell and Regenerative Medicine Innovation Institute*, *Chinese Academy of Sciences*, *Beichen West Road*, *Chaoyang District*, *Beijing* 100101, *China*
[5] *Tropical Crop Genetic Resource Research Institute*, *Chinese Academy of Tropical Agricultural Sciences*, *Haikou*, *Hainan* 571101, *China*
[6] *College of Veterinary Medicine*, *Xinjiang Agricultural University*, *Urumqi*, *Xinjiang* 830052, *China*

## ABSTRACT

Gastrointestinal symptoms frequently accompany anemia caused by *HBB* mutations, such as β-thalassemia; however, the mechanisms linking disordered hemoglobin biology to intestinal dysfunction remain incompletely understood. In this study, *HBB*-mutant cynomolgus monkeys were generated and analyzed together with wild-type (WT) controls through integrated metabolomic and metagenomic profiling. *HBB* mutation was associated with a marked shift in gut microbial ecology, characterized by reduced microbial diversity and altered abundances of *Lactobacillus* and *Bacteroides*. Metabolic profiling revealed broad perturbation of amino acid, lipid, energy, and immune-related metabolic pathways, with 3-oxooctadecanoic acid (HMDB0254633) emerging as a discriminative metabolite between WT and *HBB*-mutant animals. Multiomics integration indicated that *HBB* mutation reshaped microbiota-metabolite interactions and may thereby affect host metabolism and immune responses. To examine the functional relevance of this metabolite, 3-oxooctadecanoic acid was administered to C57BL/6 mice with castor oil-induced diarrhea. High-dose treatment alleviated diarrhea severity, improved stool parameters, limited body weight loss, and partially restored gut microbial composition. These findings provide non-human primate evidence that β-thalassemia-associated *HBB* mutation disrupts intestinal microbiota homeostasis and metabolic output, identifying 3-oxooctadecanoic acid as a candidate biomarker and potential regulator of gastrointestinal dysfunction. This study provides a valuable framework for understanding how host genetic variation contributes to gut microbiome remodeling and gastrointestinal manifestations in β-thalassemia.

**Keywords:** Gut microbiota; β-thalassemia; Cynomolgus monkeys; *HBB* mutants; Metabolome

## INTRODUCTION

Thalassemia caused by *HBB* mutations can lead to increased intestinal iron absorption (Heintz-Buschart & Wilmes, 2018). Intestinal mineral transport is further disturbed by impaired calcium absorption, and regulation of calcium transport in this setting highlights the close physiological interaction between calcium and iron metabolism (Lertsuwan et al., 2018). These abnormalities occur in parallel with iron overload, persistent inflammation, and oxidative stress, all of which can reshape the intestinal microenvironment and influence host-microbiota interactions (Gu et al., 2023; Malesza et al., 2022). Accumulating evidence has indicated that gut microbial communities differ substantially between thalassemia patients and healthy individuals, including enrichment of potentially pathogenic taxa and depletion of commensal bacteria

Received: 09 September 2025; Accepted: 05 March 2026; Online: 06 March 2026

Foundation items: This work was supported by the Hainan Academy of Agricultural Sciences Science and Technology Innovation Project (HAAS2025KJCX13) and Research Startup Fund Project for Introduced Talent at the Hainan Academy of Agricultural Sciences (HNXM2024RCQD06).

[#]Authors contributed equally to this work

*Corresponding authors, E-mail: yangsh@scau.edu.cn; 13250732023@163.com

This is an open-access article distributed under the terms of the Creative Commons Attribution Non-Commercial License (http://creativecommons.org/licenses/by-nc/4.0/), which permits unrestricted non-commercial use, distribution, and reproduction in any medium, provided the original work is properly cited.

Copyright ©2026 Editorial Office of Zoological Research, Kunming Institute of Zoology, Chinese Academy of Sciences

associated with intestinal homeostasis (Djulejic et al., 2024; Nonejuie et al., 2024). Accordingly, microbiota-directed strategies have attracted interest as adjunctive approaches for thalassemia management, although large-scale clinical studies are still needed to validate their safety and efficacy. Current work examining probiotics, including *Lactobacillus* and *Bifidobacterium* species, has begun to evaluate effects on iron metabolism and inflammatory markers in patients with thalassemia (Frąckowiak et al., 2025; Ul Ain et al., 2024). Although fecal microbiota transplantation has been proposed as a potential therapeutic strategy (Yadegar et al., 2024), precision microbiome interventions for thalassemia will require patient-stratified multiomics analyses that integrate metagenomic and metabolomic data to define disease-associated microbial and metabolic alterations.

The gut microbiome is essential for host metabolism, immune function, and physiological homeostasis, and has emerged as a key modulator of disease susceptibility and progression (He et al., 2022; Thursby & Juge, 2017). Disruption of gut microbial ecology is associated with metabolic syndrome, diabetes, inflammatory bowel disease, obesity, and neurological disorders (Turnbaugh et al., 2006), emphasizing the need to define how microbial communities interact with host genetic and metabolic networks to shape disease phenotypes (Shalon et al., 2023). Fecal metagenomics and metabolomics provide complementary resolution of these interactions by linking microbial composition and functional potential to metabolite production and host metabolic state (Nicholson et al., 2012). Integrated multiomics therefore enables systematic analysis of how genetic variation alters gut microbial structure, microbial function, and metabolite profiles, providing a framework xfor resolving the interactions among genes, microbes, and metabolic pathways in complex disease (Glenn & Mowry, 2016; Groussin et al., 2017). For instance, in diabetic mice, metabolomic studies have linked gut microbiota-derived short-chain fatty acids to insulin sensitivity (Nicholson et al., 2012), whereas broader microbiome research has implicated microbial regulation of energy metabolism in obesity, metabolic syndrome, and hematological disorders such as sickle cell anemia (Turnbaugh et al., 2006). Microbial metabolism of dietary fiber has also been shown to influence allergic airway disease and hematopoiesis, highlighting systemic effects of intestinal microbial activity beyond the gastrointestinal tract (Trompette et al., 2014). These integrated approaches can further identify disease-associated biomarkers with potential value for disease diagnosis, prevention, and therapeutic development (Galié et al., 2021).

Mouse models have been indispensable for exploring the relationship between gut microbial communities and host health, yet species-specific differences substantially limit direct extrapolation to human physiology. Notably, mice differ from humans in genetic background, intestinal anatomy, luminal biochemistry, regional pH, gut size, mucus composition, and microbial habitat structure, all of which can influence microbiome assembly and host-microbe interactions (Hugenholtz & De Vos, 2018). Non-human primates, particularly cynomolgus monkeys, offer a more translationally relevant platform for gut microbiome research than rodent models because they more closely approximate humans in genome organization, immune architecture, metabolic regulation, gastrointestinal physiology, and microbial community structure (Ebeling et al., 2011; Zhang et al., 2024b; Sun et al., 2025; Yuan et al., 2025). These similarities support more accurate modeling of human disease mechanisms, host-microbiota interactions, and therapeutic responses, thereby providing critical physiological and pathological context for studying microbiome-associated disease processes.

In this study, we hypothesized that β-thalassemia is associated with significant alterations in the structure and metabolic functions of the gut microbiota, thereby contributing to the gastrointestinal symptoms observed with this condition. Juvenile *HBB*-deficient cynomolgus monkeys were compared with control monkeys using fecal metagenomic and metabolomic profiling to define the impact of *HBB* deficiency on microbial composition, functional pathways, and metabolic output. A disease-associated differential metabolite was further evaluated in a castor oil-induced diarrhea mouse model to determine whether it exerted a protective effect against intestinal dysfunction and could serve as a candidate biomarker. By integrating fecal multiomics from juvenile *HBB*-mutant and control cynomolgus monkeys with functional validation in a diarrhea mouse model, this study establishes a translational framework for investigating gene-microbiota-host interactions and highlights the value of non-human primates for modeling complex disease mechanisms.

## MATERIALS AND METHODS

### Animals, sample collection, and storage

All cynomolgus monkeys were supplied and maintained by Guangdong Blue Island Biotechnology Co., Ltd. (GBIB, China), an accredited member of the Association for Assessment and Accreditation of Laboratory Animal Care International. All animal procedures were performed in accordance with the Guide for the Care and Use of Laboratory Animals and approved by the Institutional Animal Care and Use Committee of GBIB (Approval No. LD2017-003). Six-month-old cynomolgus monkeys were used, including three wild-type (WT) animals and five *HBB*-deficient animals. Male monkeys weighed approximately 2 kg, whereas female monkeys weighed approximately 1.5 kg. *HBB*-mutant monkeys were generated in a previous study (Huang et al., 2019), and all procedures followed ARRIVE guidelines. Health status was validated through comprehensive health records and veterinary examination before the experiment. Macaques were housed at 26°C under 30%–70% humidity and a 12 h:12 h light/dark cycle, with lights on at 0700h and off at 1900h to simulate natural day-night length. Animals were provided *ad libitum* access to drinking water and a diet comprising formulated feed supplemented with fresh vegetables and fruit. Fresh fecal samples were collected from WT and *HBB* gene-edited macaques, immediately frozen in liquid nitrogen, stored at −80°C, and transported on dry ice to BGI Genomics for processing and analysis.

Healthy C57BL/6 WT mice aged 6–8 weeks and weighing 20–24 g were purchased from Vital River Laboratory Animal Co. (Beijing, China). Equal numbers of male and female mice were housed under environmentally controlled conditions at 22°C with a 12 h:12 h light/dark cycle (lights on from 0700 h to 1900 h) and *ad libitum* access to standard laboratory chow and water.

### Metagenomic sequencing

Metagenomic sequencing was performed on the BGI DNBSEQ-T7 platform using the PE150 strategy. High-quality

clean reads were generated, assembled into contigs, and further processed for gene prediction and functional annotation.

**Metabolite extraction**

Samples were thawed slowly at 4°C, and 25 mg of each sample was transferred into a 1.5 mL Eppendorf tube. Subsequently, 800 μL of precooled (−20°C) extraction solution (methanol:acetonitrile:water; 2:2:1, v:v:v), 10 μL of internal standard, and two small steel beads were added to each tube. Samples were homogenized in a tissue grinder at 50 Hz for 5 min, sonicated in an ice-water bath at 4°C for 10 min, and centrifuged at 25 000 ×*g* for 15 min at 4°C. The supernatant (600 μL) was collected, concentrated under vacuum, and reconstituted in 600 μL of reconstitution solution (methanol:water; 1:9, v:v). After vortexing for 1 min and sonication at 4°C for 10 min, samples were centrifuged again at 25 000 ×*g* for 15 min at 4°C, and the resulting supernatants were transferred to sample vials. For quality control analysis, 50 μL of supernatant from each sample was pooled to generate a mixed quality control sample.

**Ultra-performance liquid chromatography-mass spectrometry (UPLC-MS)**

Metabolite separation and detection were performed on a Waters UPLC I-Class Plus system (Waters, USA) coupled to a Q Exactive high-resolution mass spectrometer (Thermo Fisher Scientific, USA).

**Chromatographic conditions**: Metabolites were separated on a BEH C18 column (1.7 μm, 2.1 mm×100 mm, Waters, USA). In positive ion mode, mobile phase A consisted of 0.1% formic acid in water, and mobile phase B consisted of 0.1% formic acid in methanol. In negative ion mode, mobile phase A consisted of 10 mmol/L ammonium formate in water and mobile phase B consisted of 95% methanol. Gradient elution was performed as follows: 0–1 min, 2% B; 1–9 min, 2% to 98% B; 9–12 min, 98% B; 12–12.1 min, 98% B to 2% B; 12.1–15 min, 2% B. The flow rate was set to 0.35 mL/min, the column temperature was maintained at 45°C, and the injection volume was 5 μL.

**Mass spectrometric conditions**: Mass spectrometric data were acquired on a Q Exactive mass spectrometer (Thermo Fisher Scientific, USA) in full-scan and MS/MS modes. The mass-to-charge ratio (m/z) scan range was 70–1 050, with a resolution of 70 000 for MS and 17 500 for MS/MS. The automatic gain control (AGC) target was 3e6 for MS and 1e5 for MS/MS. The maximum injection time was 100 ms for MS and 50 ms for MS/MS. Fragmentation was performed using the top three precursor ions selected according to ion intensity, with fragmentation energies of 20, 40, and 60 eV.

**Software and parameters**

All samples were sequenced on the BGI DNBSEQ-T7 platform using the PE150 strategy, with at least 8 Gb of clean reads generated per sample. Libraries were prepared with the MGIEasy Universal DNA Library Prep Kit v.3.0 after random fragmentation using Covaris M220 and publicly available adapter sequences. Quality control was performed with SOAPnuke v.2.1.6. Host-derived reads were removed by alignment to the *Macaca_fascicularis*_5.0 reference genome using Bowtie2 v.2.2.5. Assembly, gene prediction, and sequence deduplication were performed with MEGAHIT v.1.2.9, MetaGeneMark v.3.38, and CD-HIT v.4.8.1, respectively, using fixed parameters. Taxonomic and functional annotations were performed with Kraken2 and Bracken against the NCBI NT database (release 2023-06-21) and with DIAMOND alignment against KEGG v.104.0, eggNOG v.5.0, and CAZy 2023-07, followed by pathway mapping with HUMAnN v.3.6. Diversity and differential abundance analyses were conducted with QIIME2 v.2023.2, LEfSe v.1.1.0, and DESeq2 v.1.34.0. All software versions and databases were fixed and publicly deposited to ensure full reproducibility.

**Library construction and sequencing**

DNA was extracted from fecal samples, and metagenomic DNA was randomly fragmented with a Covaris ultrasonic processor. DNA fragments (200–400 bp) were selected using magnetic beads and subjected to end repair, A-tailing, and adapter ligation. Polymerase chain reaction (PCR) amplification was performed, followed by circularization of amplified products. Uncircularized linear DNA molecules were digested to obtain the final sequencing library.

**Data processing**

Raw sequencing reads were filtered and processed using SOAPnuke v.2.1.6 and SAMtools v.1.2. Reads were discarded if they contained more than 10% undetermined bases (N bases), adapter sequences of at least 15 bases, or more than 50% low-quality bases (Q<20). Host-derived sequences were removed using Bowtie2 v.2.2.5, and the remaining high-quality reads were retained as clean data.

All raw sequence data generated in this study were deposited in the Science Data Bank, NCBI database, and the Genome Sequence Archive (GSA) of the National Genomics Data Center (Genomics, Proteomics & Bioinformatics 2021; Nucleic Acids Res 2022), China National Center for Bioinformation/Beijing Institute of Genomics, Chinese Academy of Sciences. The data are publicly accessible at https://ngdc.cncb.ac.cn/gsa (Chen et al., 2021).

**Metagenomic assembly**

Clean reads that passed quality control were assembled *de novo* using MEGAHIT. Contigs shorter than 200 bp were excluded from further analysis.

**Gene prediction and abundance information**

Genes were predicted from metagenomic assemblies using MetaGeneMark. Redundant sequences were removed with CD-HIT by clustering sequences at 95% identity and 90% coverage thresholds. Representative sequences from each cluster were retained to construct the nonredundant gene set. Gene abundance was quantified using Salmon, and transcripts per million (TPM) values were used to estimate gene abundance.

**Gene function prediction**

Functional annotation of nonredundant genes was performed with DIAMOND using BLASTP searches against reference protein databases.

**Species annotation and abundance calculation**

Taxonomic annotation was performed with Kraken2 using default parameters and the NCBI NT database (release 2023-06-21). Species-level abundance in the metagenomic samples was estimated with Bracken using Bayesian algorithms based on Kraken classification results.

**Species diversity analysis**

Microbial diversity was assessed in R. In brief, α-diversity was

evaluated using the Chao1, Shannon, and Simpson indices. β-diversity was estimated using Bray-Curtis distance and Jensen-Shannon divergence to quantify differences in microbial community structure among samples and groups.

**Castor oil-mediated induction of diarrhea**

Mice were housed separately and randomly assigned to four different groups, with 10 mice per group. Diarrhea was induced by intragastric administration of castor oil at 20 mL/kg body weight once daily at 1400h for six consecutive days. The control group received an equivalent volume of normal saline instead of castor oil. On day 3 after treatment initiation, cage bedding was replaced with appropriately sized filter paper to monitor fecal output over a 5 h period, during which diarrheal symptoms were documented.

The control group received normal saline at 10 mL/kg body weight. The castor oil group (CO) received castor oil at 20 mL/kg body weight by intragastric administration to induce diarrhea. The 3-oxooctadecanoic acid (3_AO) low-dose (3_AOL) and high-dose (3_AOH) groups received 3_AO at 1.0 mL/kg and 2.0 mL/kg, respectively. The positive-control group (3_AOMP) received montmorillonite powder at 3.0 g/kg (0.3 g/mL). All test substances were administered intragastrically at 0900h once daily over four consecutive days.

Fecal analysis included quantification of total defecation events and loose stools, followed by calculation of the loose stool rate, stool consistency grade, and diarrhea index according to established methods (Zhu et al., 2022). The loose stool rate was calculated as the proportion of unformed stools relative to total fecal output. Stool consistency was classified based on the diameter of fecal stains left on the filter paper: (1) <1 cm, (2) ≥1 cm but <1.9 cm, (3) ≥2 cm but ≤3 cm, and (4) >3 cm. For irregularly shaped stains, the mean of the longest and shortest diameters was used. The diarrhea index was derived by multiplying the loose stool rate by the stool consistency grade.

## RESULTS

**Fecal metabolomic profiling identifies distinct metabolic signatures in *HBB*-mutant cynomolgus monkeys**

Fecal samples were collected from 6-month-old *HBB*-mutant cynomolgus monkeys and age-matched WT controls for integrated metabolomic and metagenomic analysis (Figure 1A). The generation and characterization of *HBB*-mutant monkeys were described previously (Huang et al., 2019) and are summarized in Figure 1B–F. Integration of these two omics approaches enabled assessment of microbial and metabolic alterations associated with *HBB* mutation. Abundant ion peaks were detected in both positive and negative ion modes, indicating sufficient metabolite coverage for downstream analysis (Supplementary Figure S1A). Identified metabolites were quantified and classified according to Final Class annotations (Supplementary Figure S1B, C), followed by statistical categorization based on KEGG metabolic pathway assignments (Super Pathways).

Lipid-associated metabolites were further categorized according to Sub Pathways. Among fecal metabolites detected in 6-month-old cynomolgus macaques, amino acid metabolism represented the largest pathway category, with 72 metabolites accounting for 28% of all annotated metabolites. Lipid metabolism included 37 metabolites, accounting for 15%, whereas biosynthesis of other secondary metabolites included 34 metabolites, representing 13% (Figure 2A). These results identified amino acid and lipid metabolism as the predominant metabolic pathway categories in fecal metabolite profiles from WT and *HBB*-mutant cynomolgus monkeys.

Principal component analysis (PCA) was performed to evaluate global metabolic variation between WT and *HBB*-mutant fecal samples. Samples from the two groups clearly separated in principal component space, indicating distinct fecal metabolomic profiles between WT and *HBB* mutants (Figure 2B). Univariate analysis was then performed using fold change (FC)≥1.2 and $P$<0.05 as screening criteria. Compared with the WT group, *HBB*-mutant monkeys showed 177 significantly up-regulated metabolites and 233 significantly down-regulated metabolites (Figure 3C, D). To further assess the expression patterns of these differential metabolites, metabolite abundance data were first $\log_2$-transformed and standardized by $Z$-score normalization (zero-mean normalization), followed by hierarchical clustering analysis based on Euclidean distance. The 410 differential metabolites exhibited pronounced intergroup separation, with consistent abundance patterns within WT and *HBB*-mutant samples (Figure 3E). These findings indicate that *HBB* mutation is associated with substantial remodeling of fecal metabolite composition in juvenile cynomolgus monkeys.

**Abnormal patterns of metabolites in *HBB* mutants**

To define coordinated changes among differential metabolites, Spearman correlation coefficients were calculated for metabolite pairs, and associations with $|r|$>0.8 and $P$<0.05 were retained for construction of a correlation chord diagram. Metabolites classified as “Amino acids, peptides, and analogues” were negatively correlated with metabolites in the “Organic acids” category, whereas most other metabolite classes showed positive correlations (Figure 3A). A correlation heatmap was further generated for the top 20 differential metabolites ranked by the smallest $P$-values. Among these metabolites, HMDB006217 showed a negative correlation pattern, whereas the remaining 19 metabolites showed positive correlations (Supplementary Figure S2A).

KEGG-based pathway enrichment analysis was then performed for the differential metabolites, and the top 10 most significantly enriched pathways were visualized ($P$<0.05). ABC transporters, phenylalanine metabolism, linoleic acid metabolism, and biosynthesis of amino acids contained the largest numbers of enriched differential metabolites and showed highly significant enrichment ($P$<0.01) (Figure 3B; Supplementary Figure S2B). To evaluate directional pathway-level changes, Differential Abundance Score analysis was applied to the top 10 significantly enriched pathways in both groups. In the “Intestinal immune network for IgA production”, “Small cell lung cancer”, and “Th17 cell differentiation” pathways, one metabolite in each pathway was significantly up-regulated in *HBB* mutants. In contrast, both metabolites assigned to “Alanine, aspartate, and glutamate metabolism” and the “Pentose phosphate pathway” were significantly down-regulated in *HBB* mutants. All three metabolites in the “Linoleic acid metabolism” pathway were also significantly down-regulated. In addition, metabolites assigned to “ABC transporters” and “Phenylalanine metabolism” showed an overall increase in abundance in *HBB* mutants (Figure 3C; Supplementary Table S1). Receiver operating characteristic (ROC) curve analysis further identified HMDB0254633 as a discriminative metabolite, with an area under the curve (AUC)

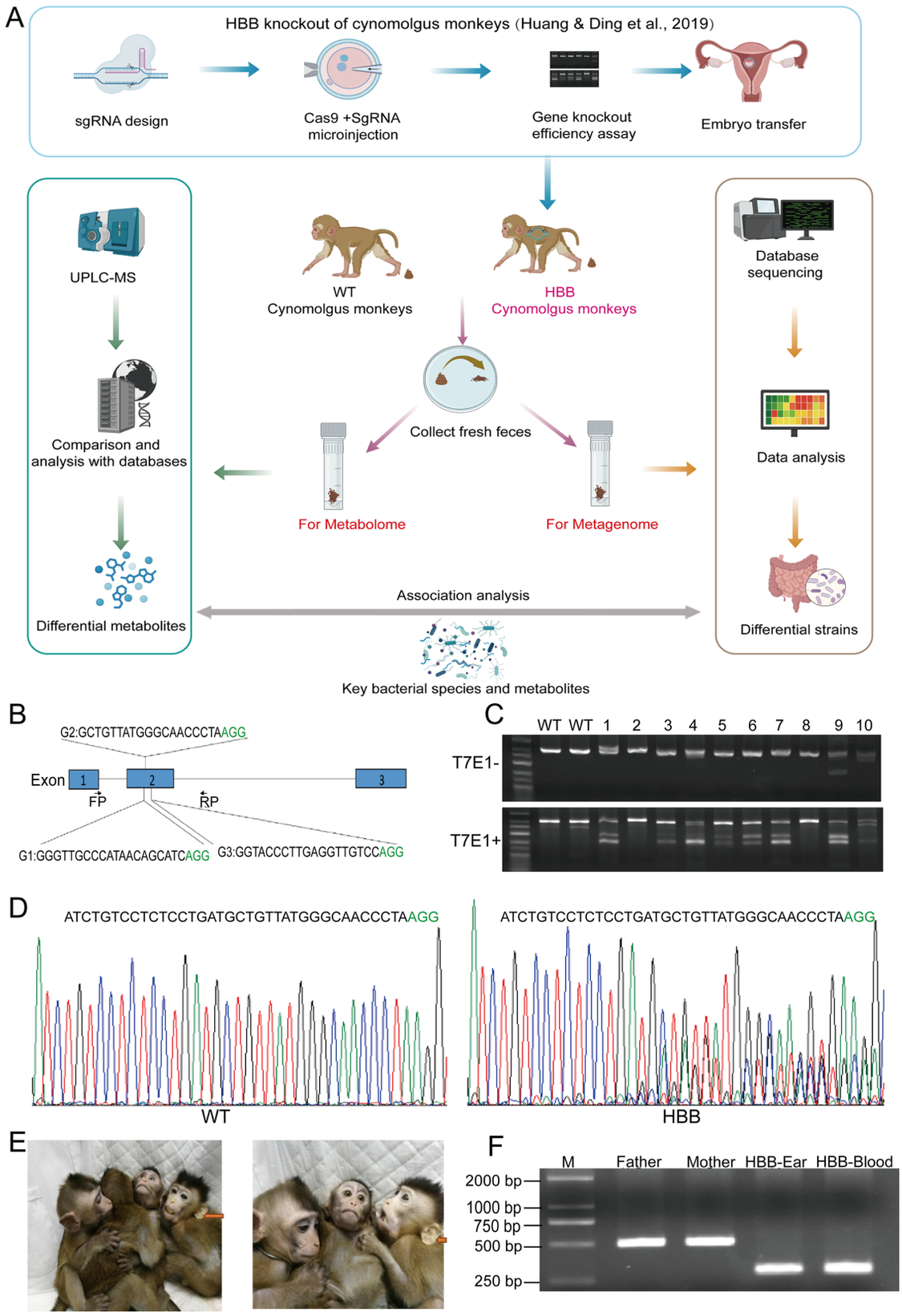



**Figure 1 Experimental workflow and generation of *HBB* gene-edited cynomolgus monkeys**

A: Workflow for fecal metagenomic and metabolomic analyses. B: Schematic showing target site selected for *HBB* gene disruption. Cynomolgus monkey *HBB* gene is located on chromosome 14, and the knockout site was selected according to gene structure and transcriptional features. C: T7E1 digestion analysis of blastocysts. T7E1− indicates gel electrophoresis without T7E1 enzyme treatment; T7E1+ indicates gel electrophoresis after T7E1 enzyme treatment. Numbers 1 to 10 indicate embryo identifiers. D: Sanger sequencing results. Peak colors denote bases as follows: black, G; blue, C; green, A; and red, T. E: Representative images of *HBB* mutants and control macaques at 4 months of age. Red arrow indicates electrophoretic analysis of ear tissue and blood from knockout monkey.

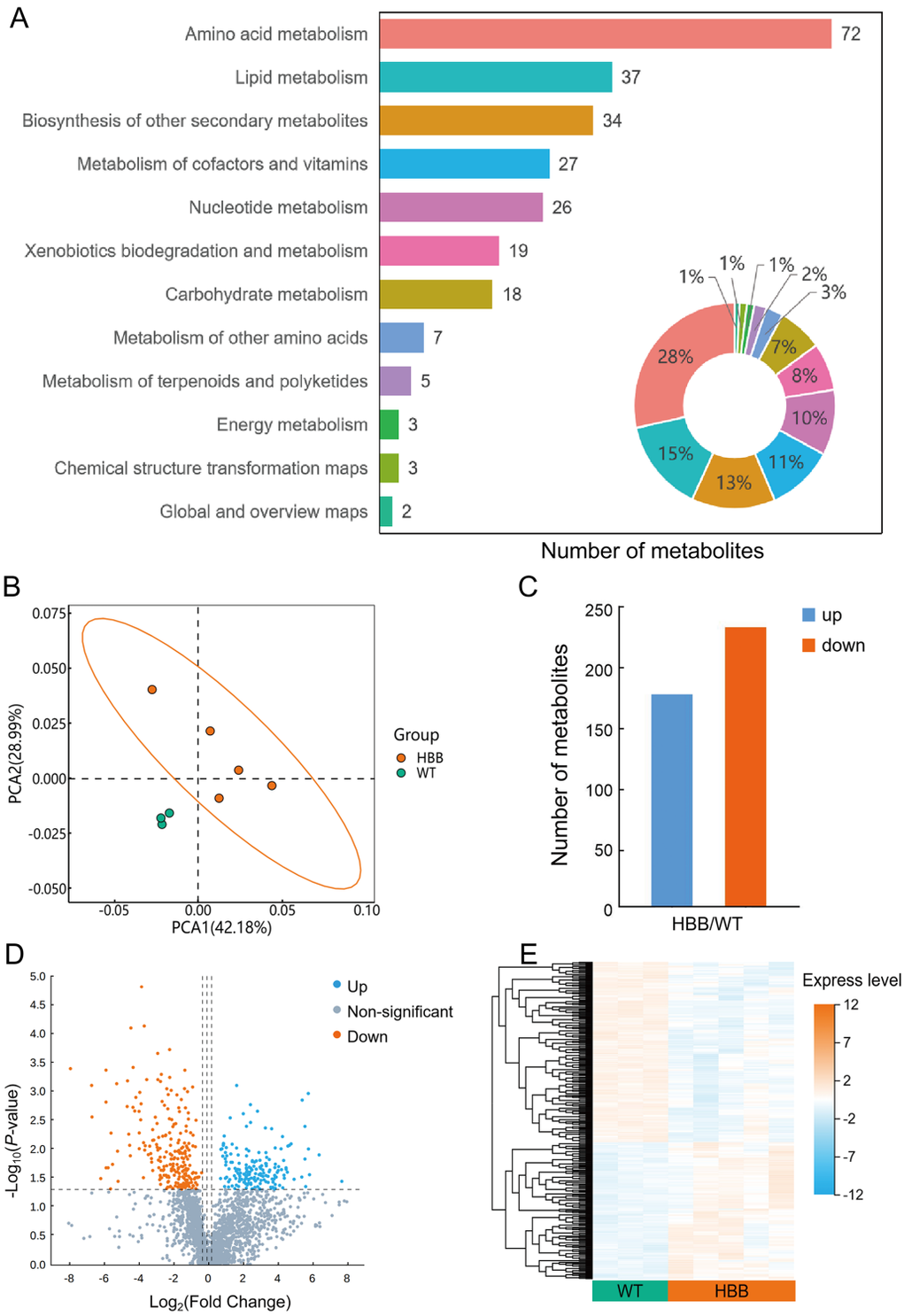



**Figure 2 Differential metabolite screening**

A: KEGG pathway classification of metabolites. Y-axis shows metabolic pathway categories, and x-axis shows number of metabolites. Colors represent metabolic pathway categories, and percentages indicate proportion of metabolites within each category among all metabolites with pathway annotations. B: PCA clustering plot. X-axis and y-axis represent the first and second principal components (PC1 and PC2), respectively, with values in parentheses indicating variance explained by each component. Each point represents one sample, with green and yellow indicating WT macaques and *HBB* mutants, respectively. Ellipses represent 95% confidence intervals. C: Bar plot of significantly differential metabolites. X-axis represents group comparison, and y-axis indicates number of differential metabolites. Blue bars represent significantly Up-regulated metabolites, and orange-yellow bars represent significantly Down-regulated metabolites. D: Volcano plot of differential metabolites. X-axis represents $\log_2$-transformed Fold Change, and y-axis represents $-\log_{10}$-transformed *Q*-value (*P*-value). Blue points represent significantly down-regulated metabolites, orange-yellow points represent significantly up-regulated metabolites, and non-significant metabolites are shown in gray. E: Heatmap of differential metabolite abundance. Each row represents a differential metabolite, and each column represents a sample. Colors indicate abundance levels, with green to red representing low to high abundance.

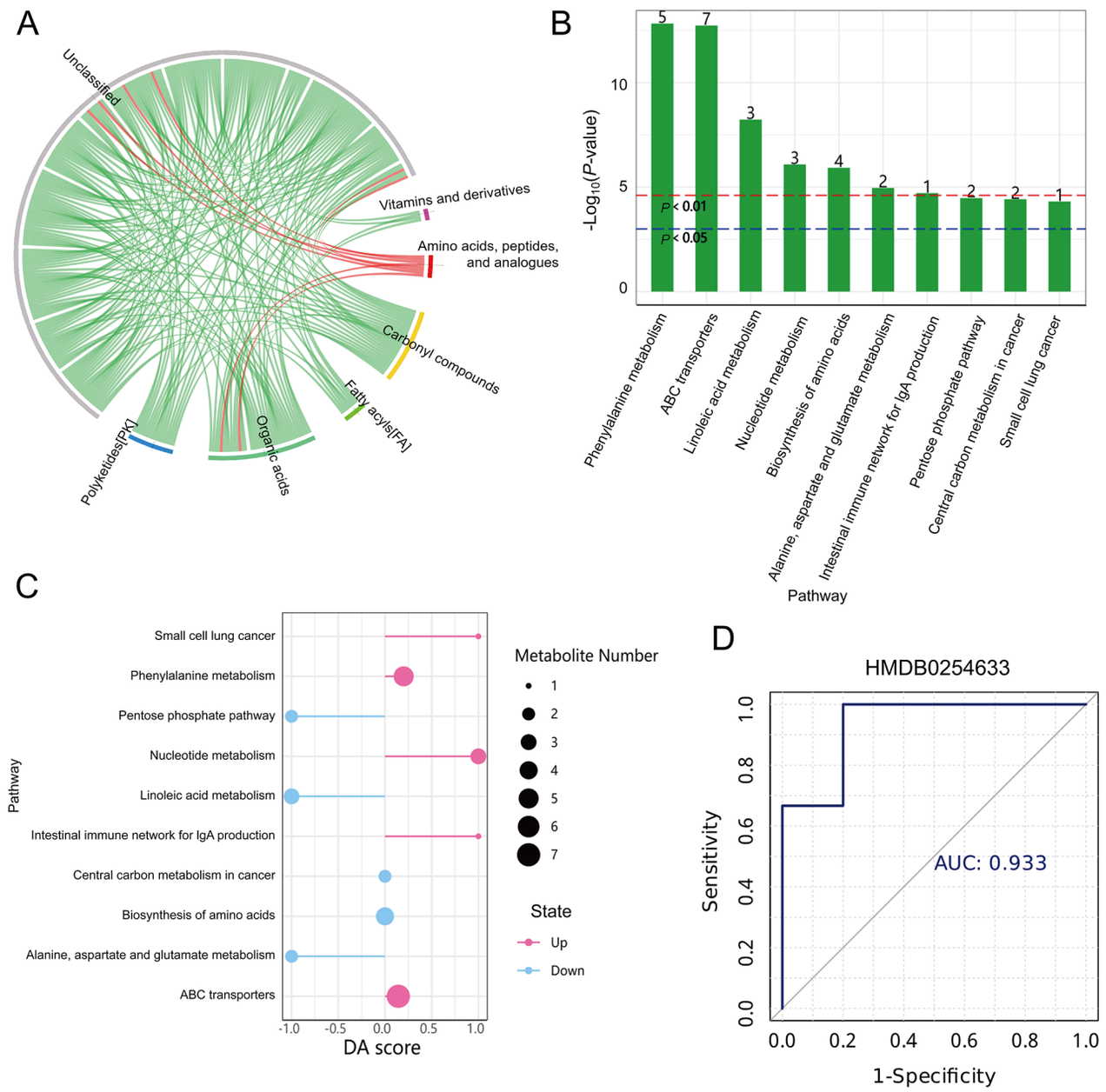



**Figure 3 Differential metabolite analysis**

A: Chord diagram showing correlations among differential metabolites. Links in inner circle represent differential metabolites, and arcs in outer circle denote metabolite categories. Colored lines indicate correlation within each class of metabolites, with green lines representing positive correlations and red lines representing negative correlations. B: Bar plot of pathway enrichment analysis. Pathways above the red dashed line reached $P$<0.01, and pathways above the blue dashed line reached $P$<0.05. Numbers on bars indicate number of differential metabolites annotated to each metabolic pathway. C: Score plot of pathway enrichment analysis. Y-axis shows metabolic pathways, and x-axis shows differential abundance score (DAscore). A score of 1 indicates that all differential metabolites annotated to that pathway are up-regulated, while a score of −1 indicates down-regulation. Line length represents absolute DAscore, and dot size at the endpoint reflects number of metabolites in the pathway, with larger dots indicating more metabolites. D: Receiver operating characteristic (ROC) curve. X-axis represents 1-specificity, and y-axis represents sensitivity. Area under the curve (AUC) is shown by the area below the line.

of 0.933, indicating strong potential as a biomarker for distinguishing WT from *HBB* mutants (Figure 3D).

### Abnormal gut microbiota composition in *HBB*-deficient cynomolgus macaques

Quality-controlled metagenomic reads from each sample were assembled using MEGAHIT, and contigs shorter than 300 bp were removed before downstream analysis. Assembly quality was evaluated using continuity and completeness metrics, including assembly length, maximum contig length, N50, N90, and minimum contig length (Supplementary Table S2). After quality control, assembly, and gene prediction, metagenomic gene catalogs were generated for all samples. Predicted gene fragments were predominantly distributed between 200 and 1 499 bp (Supplementary Figure S3A). Gene-level α-diversity, assessed using the Chao1, Shannon, and Simpson indices, did not differ significantly between the *HBB*-deficient and WT groups, indicating comparable gene richness, evenness, and diversity (Supplementary Figure S3B). Gene-level β-diversity also showed no significant intergroup differences, and within-

group dispersion remained within an acceptable range (Supplementary Figure S3C).

Species accumulation curves were then used to measure and predict the trend of species richness in the community as sample size increased. Curves for both WT and *HBB*-deficient macaques approached a plateau, indicating adequate sampling coverage for community-level diversity (Figure 4A). Species-level α-diversity analysis revealed that the Chao1 index differed significantly between the two groups ($P$=0.036), indicating altered microbial richness in feces from *HBB* gene-edited macaques (Figure 4B). In contrast, Shannon and Simpson indices did not differ significantly between groups. However, median values for both indices were higher in the WT group than in the *HBB*-deficient group, suggesting a modest reduction in fecal microbial evenness and overall community diversity in *HBB* gene-edited macaques (Supplementary Figure S3D). β-diversity analysis was performed to examine differences in microbial community composition between groups. Partial least squares discriminant analysis (PLS-DA) indicated partial separation between the *HBB*-deficient and WT groups, although differences did not reach statistical significance (Figure 4C; Supplementary Figure S3E). Together, these findings indicate that *HBB* deficiency affected species richness in the fecal microbiota of cynomolgus macaques, whereas changes in overall community evenness and β-diversity were comparatively limited.

**Abnormal gut microbiota profiles in *HBB*-deficient cynomolgus macaques**

Species-level Venn analysis of fecal microbiota identified 3 653 shared species between WT and HBB-mutant macaques, with 185 species unique to *HBB* mutants and 996 species unique to WT macaques (Figure 5A). Taxonomic profiling across phylum, genus, and species levels revealed marked compositional differences between groups. At the phylum level, Firmicutes dominated the fecal microbiota in both WT and *HBB*-mutant macaques (Figure 5B). At the species level, *Faecalibacterium prausnitzii* was the most abundant taxon in both groups but showed a higher abundance in *HBB* mutants than in WT monkeys. Conversely, two highly abundant *Lactobacillus* species, *Lactobacillus reuteri* and *Lactobacillus johnsonii*, were reduced in *HBB* mutants compared to WT macaques (Figure 5C). At the genus level, *Prevotella* and *Faecalibacterium* were enriched in *HBB* mutants, whereas *Lactobacillus* showed the highest abundance in WT monkeys and was markedly reduced in *HBB* mutants (Supplementary Figure S3F).

Differential abundance analysis further confirmed genotype-

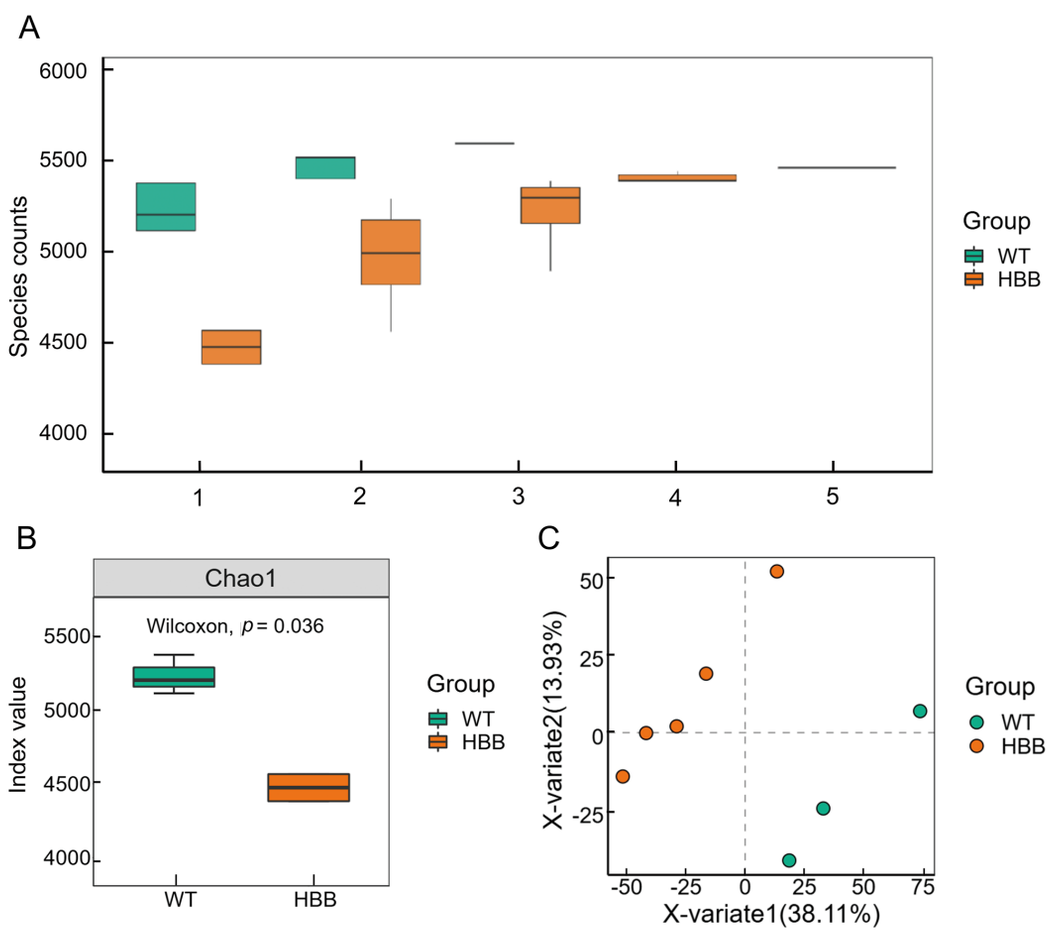



**Figure 4 Gut microbiota diversity analysis**

A: Species rarefaction curve box plot. X-axis represents number of samples, and y-axis represents number of species (detected species count). Box color represents groupings. B: Species α-diversity Chao1 box plot. X-axis represents groups, and y-axis shows index values. $P$<0.05 indicates significant differences in α-diversity between groups. C: PLS-DA analysis scatter plot. Each point represents one sample, with blue points representing WT group and yellow points representing *HBB* mutants. X-axis and y-axis represent PLS dimensions that separate the samples, and values in parentheses indicate explained variance of the reduced dimensions for the samples.

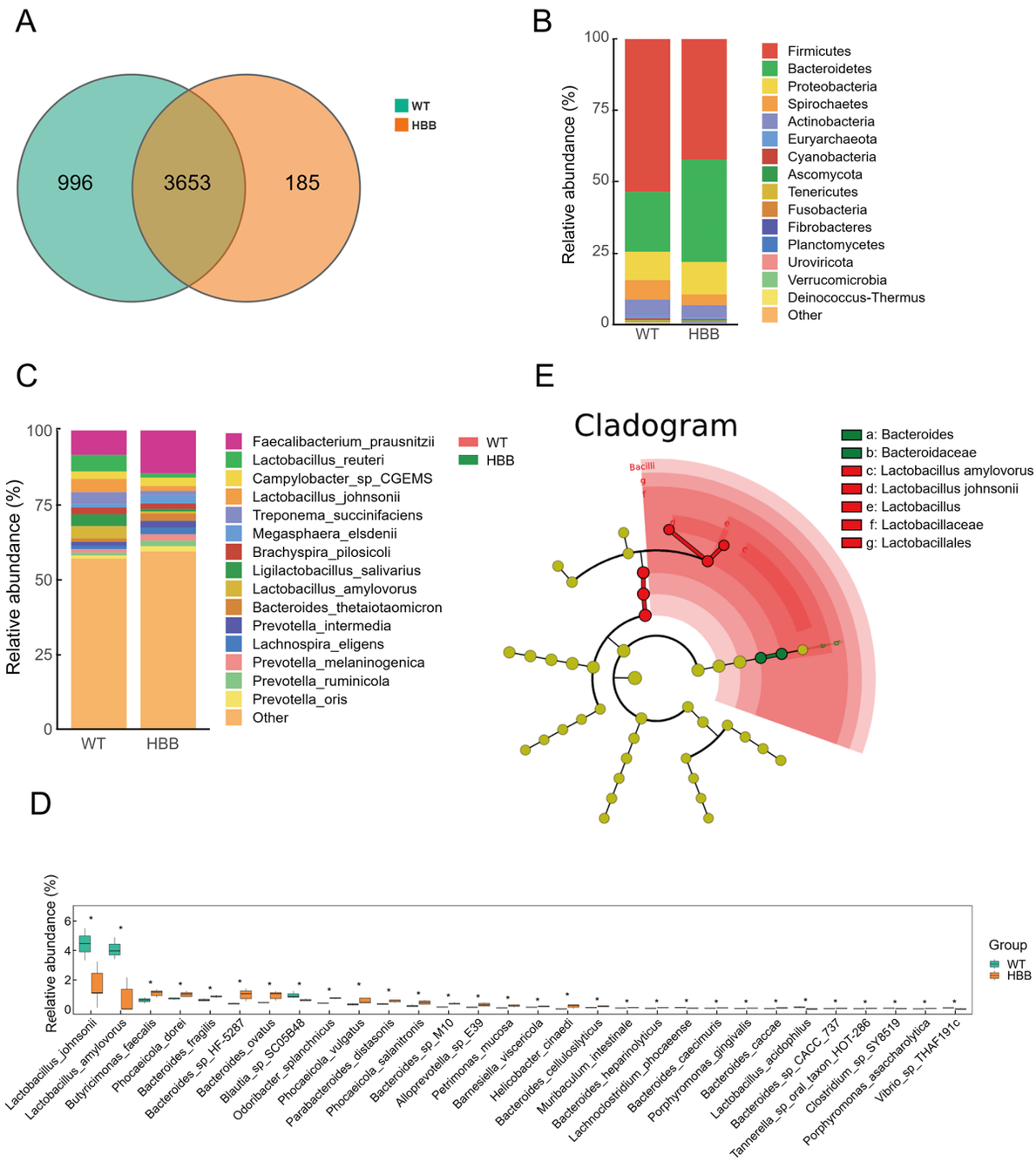



**Figure 5 Differential gut microbiota analysis**

A: Species-level Venn diagram. Numbers in overlapping regions represent species shared between groups, whereas numbers in non-overlapping regions represent species unique to each group. B: Phylum-level taxonomic abundance stacked bar chart. X-axis represents groups, and y-axis represents relative abundance of species. Bar color indicates species classification. C: Species-level abundance stacked bar chart. D: Species-level abundance box plot. X-axis represents species with statistically significant differences, and y-axis represents relative abundance of each species. Asterisk (*) indicates $P<0.05$. E: LEfSe circular phylogenetic tree. Each point represents a specific species classification, and point size corresponds to its relative abundance. Species with significant differences are colored by group, and fan colors represent higher-level species classifications.

associated shifts in fecal microbial composition. At the species level, *Lactobacillus johnsonii* and *Lactobacillus amylovorus* were the most abundant species that differed significantly between groups ($P<0.05$), with higher relative abundances in WT monkeys than in *HBB* mutants (Figure 5D). At the genus level, *Bacteroides* and *Lactobacillus* represented the most abundant differentially enriched genera. *Bacteroides* was significantly enriched in *HBB* mutants, whereas *Lactobacillus* was significantly enriched in WT monkeys (Supplementary Figure S3G).

Linear discriminant analysis effect size (LEfSe) analysis was then performed for the top eight taxa with the highest relative abundance using an LDA threshold of 2. This analysis identified *Bacteroides* as a discriminatory genus enriched in *HBB* mutants and *Lactobacillus* as a discriminatory genus enriched in WT monkeys. *Lactobacillus johnsonii* and *Lactobacillus amylovorus* also differed significantly between groups, with substantially higher abundance in WT monkeys than in *HBB* mutants (Figure 5E). These findings indicate that HBB deficiency is associated with distinct remodeling of fecal

microbiota composition, particularly involving depletion of *Lactobacillus* and related species.

**Functional alterations in fecal microbiota from *HBB*-deficient cynomolgus macaques**

To determine whether *HBB* deficiency is associated with altered microbial functional capacity, nonredundant genes predicted from fecal metagenomic data from WT and *HBB*-deficient macaques were subjected to functional annotation. KEGG-based functional enrichment analysis revealed that the dominant microbial functional categories in both groups were primarily related to carbohydrate metabolism, lipid metabolism, cofactor and vitamin metabolism, and energy metabolism (Figure 6A). Variation in the abundance of KEGG-enriched metabolic pathways was further visualized using a Circos plot (Figure 6B), which showed enrichment of K07133 and K21572 in *HBB* mutants, whereas K07729 and K07497 were less abundant than in WT animals.

Module-level KEGG enrichment analysis identified additional functional divergence between groups. Microbial genes enriched in WT monkeys were primarily associated with carbohydrate metabolism, amino acid metabolism, and translation, with significant pathway-level differences defined by |Reporter score|>1.65. In contrast, *HBB*-deficient macaques showed predominant enrichment of methane metabolism, pyruvate metabolism, and atrazine degradation, which also exceeded the significance threshold (|Reporter score|>1.65) (Figure 6C). Together, these findings indicate that HBB deficiency is associated with remodeling of gut microbial functional profiles in cynomolgus macaques, particularly across metabolic pathways involved in nutrient utilization, energy metabolism, and xenobiotic processing.

***HBB* deficiency alters gut microbial functions and metabolic pathways in cynomolgus macaques**

Integrated metabolomic and metagenomic analysis was performed to define how *HBB* deficiency affects gut microbial community structure, microbial functional capacity, metabolic pathway activity, and microbiota-host interactions. PCA based on species-level and metabolite profiles showed clear separation between WT and *HBB*-mutant macaques, with close clustering within each group, indicating substantial differences in microbial composition and fecal metabolite profiles (Figure 7A). Canonical correlation analysis (CCA) further revealed significant intergroup differences in microbial communities and metabolites (Figure 7B). Unsupervised correlation analysis revealed that HMDB0082176 was negatively correlated with the abundance of several microbial species, whereas most other differentially abundant metabolites showed positive correlations with species abundance (Figure 7C).

Associations between functional genes and metabolites were then examined to identify metabolic pathways potentially affected by *HBB* deficiency. Univariate correlation analysis showed that HMDB0082176 was negatively correlated with the K11212, K07244, and K14124 pathways, whereas other metabolites and microbial taxa were positively correlated with multiple KEGG pathways (Figure 7D). Joint analysis using an unsupervised model produced a similar association pattern, supporting consistent links among microbial composition, functional genes, and metabolite abundance (Figure 7E). Pathway enrichment analysis of functional genes and metabolites identified the “Citrate Cycle (TCA Cycle)” as a highly enriched pathway, with a high RichFactor and multiple associated microbial genes and metabolites, suggesting a central role in altered metabolic activity and microbial community structure. This pathway included the differential metabolite oxoglutaric acid (KEGG ID: C00026) and four differential genes, *porA*, *porB*, *korC*, and *oorC* (KEGG IDs: K00169, K00170, K00177, and K00627). “Folate Biosynthesis”, “Aminoacyl-tRNA Biosynthesis”, and “ABC Transporters” also showed significant enrichment based on RichFactor and Count values, suggesting that these pathways may have important regulatory roles in metabolic function and species distribution (Figure 7F). The top 10 positively and negatively correlated microbial species associated with this metabolite in the CCA correlation matrix are shown in Supplementary Table S3. Together, these findings indicate that *HBB* deficiency is associated with coordinated shifts in gut microbial functions and metabolic pathways in cynomolgus macaques, particularly across pathways involved in energy metabolism, amino acid utilization, folate metabolism, and transport processes, which may contribute to altered host metabolic regulation.

**Impact of 3-oxooctadecanoic acid on body weight in mice with castor oil-induced diarrhea**

Castor oil administration induced marked changes in fecal output, including soft, loose, and watery stools, confirming successful establishment of the diarrhea model. Control mice consistently excreted dry, pellet-like, or soft feces throughout the experimental period. In contrast, castor oil-treated mice exhibited diarrhea-associated clinical signs, including reduced activity, ruffled fur, and lethargy. The loose stool rate, stool consistency grade, and diarrhea index were significantly higher in the 3_AO group compared with the control group. By day 10, mice in the 3_AOH group showed improved general condition and slightly higher body weight than mice in the other treatment groups, with body weight approaching that of the control group (Figure 8). These findings indicate that high-dose 3-oxooctadecanoic acid effectively attenuates castor oil-induced diarrhea and partially mitigates diarrhea-associated body weight loss.

## DISCUSSION

This multiomic study used an *HBB*-deficient cynomolgus monkey model to examine how β-thalassemia-associated genetic disruption may alter gut microbial composition, microbial functional capacity, and fecal metabolite profiles. *HBB* mutations cause anemia and can be accompanied by gastrointestinal disturbance, thereby adversely affecting intestinal homeostasis. The present multiomic analysis showed that amino acid and lipid metabolism represented major fecal metabolic pathway categories in macaques and that *HBB* deficiency was associated with pronounced changes in fecal metabolite abundance. These findings suggest that altered host-microbiota metabolic exchange may contribute to the intestinal phenotype associated with *HBB* mutation.The enrichment of amino acid and lipid metabolism pathways in fecal metabolite profiles from *HBB*-deficient macaques indicates a potential metabolic interface between β-thalassemia-related systemic stress and intestinal microbial activity. Inhibition of amino acid metabolism has been examined in distinct disease contexts, including selective targeting of human leukemia stem cells(Micheletti et al., 2018), reinforcing the broader relevance of these metabolic pathways in disease biology and therapeutic response. We

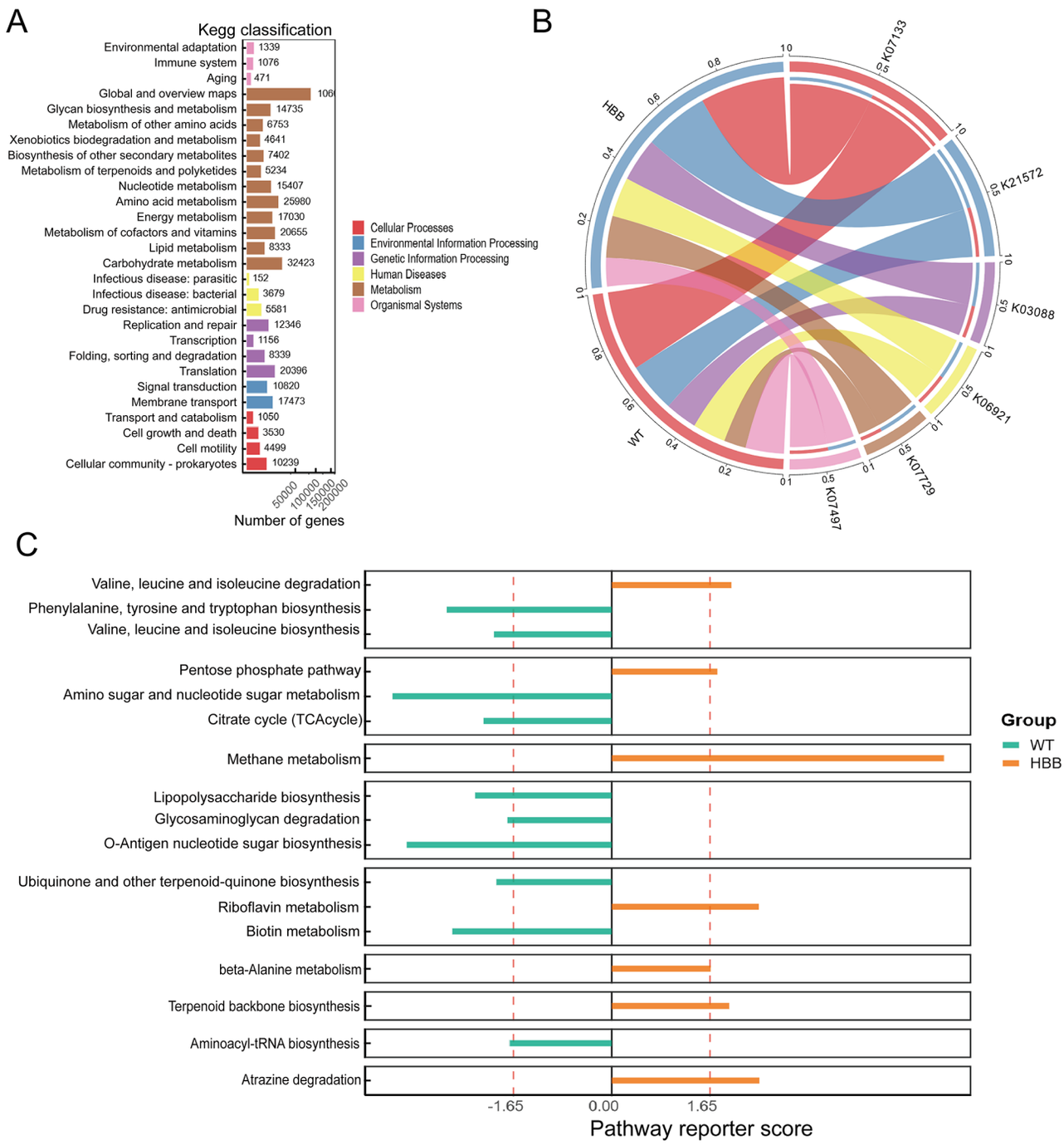



**Figure 6 Functional differential analysis**

A: Bar plot of functional gene statistics. X-axis represents number of genes, and y-axis represents functional categories. Bar colors indicate groups or functional categories. B: Circos plot of differential functions. Left side of circle represents grouping information, and right side represents functional categories. Outer scale shows the proportion of each function in the samples or ratio of different functions in the samples. Inner arc segment colors represent different groups, and connecting lines between arcs indicate the presence of that function in the sample. Arc width reflects proportion. C: KEGG pathway enrichment differential plot. X-axis represents Reporter score, and y-axis represents pathways. Dashed lines indicate the threshold for significant Reporter scores.

hypothesize that these findings may be related to thalassemia. Gut microbiota can influence systemic physiology through metabolites such as short-chain fatty acids, trimethylamine-N-oxide, bile acid derivatives, and amino acid catabolites. Human and animal studies have linked these microbial products to cardiovascular and metabolic diseases, supporting the concept that microbiome disruption can extend beyond the intestinal tract (Zhu et al., 2016). In this context, *HBB* deficiency may alter gut microbial function indirectly through changes in host metabolic demand, iron handling, immune activation, or oxidative stress, thereby shaping microbial metabolite output. Consistent with this interpretation, gut microbiome dysbiosis has been associated with abnormalities in lipid metabolism(Manolis et al., 2022; Wang et al., 2011), further supporting a mechanistic connection among microbial ecology, host metabolism, and disease-associated metabolic

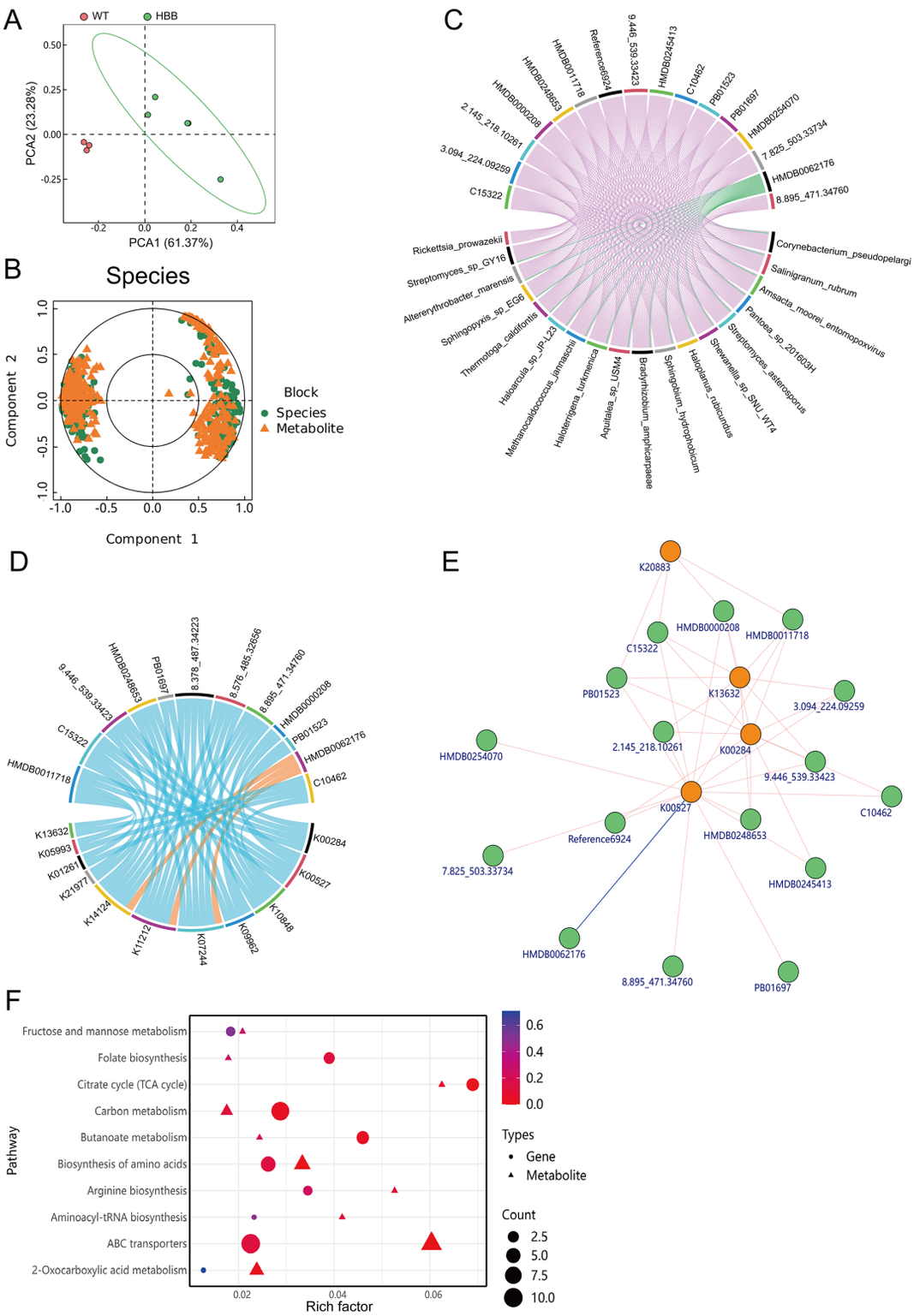



**Figure 7 Integrated metabolomic and metagenomic analysis**

A: PCA clustering plot based on integrated species and metabolite data. B: Canonical correlation analysis (CCA) plot. Inner small circles represent a correlation coefficient of 0.5, and outer large circles represent a correlation coefficient of 1. Species are represented by green dots, and metabolites are represented by orange triangles. C: Sankey diagram showing unsupervised integrated analysis of species and metabolites. Orange lines indicate negative correlations, and blue lines represent positive correlations between species and metabolites. D: Sankey diagram showing univariate correlation analysis between differential genes and metabolite functions. Green lines represent negative correlations, and purple lines represent positive correlations. E: Network analysis of differential genes and metabolite functions in an unsupervised model. Each point represents either a metabolite or an associated omics indicator. Green points represent omics indicators, and yellow points represent metabolites. Connections between points show red lines for positive correlations and blue lines for negative correlations. F: Pathway enrichment analysis of functional genes and metabolites. X-axis represents enrichment factor (RichFactor), with triangles representing functional gene pathways and circles representing metabolic pathways.

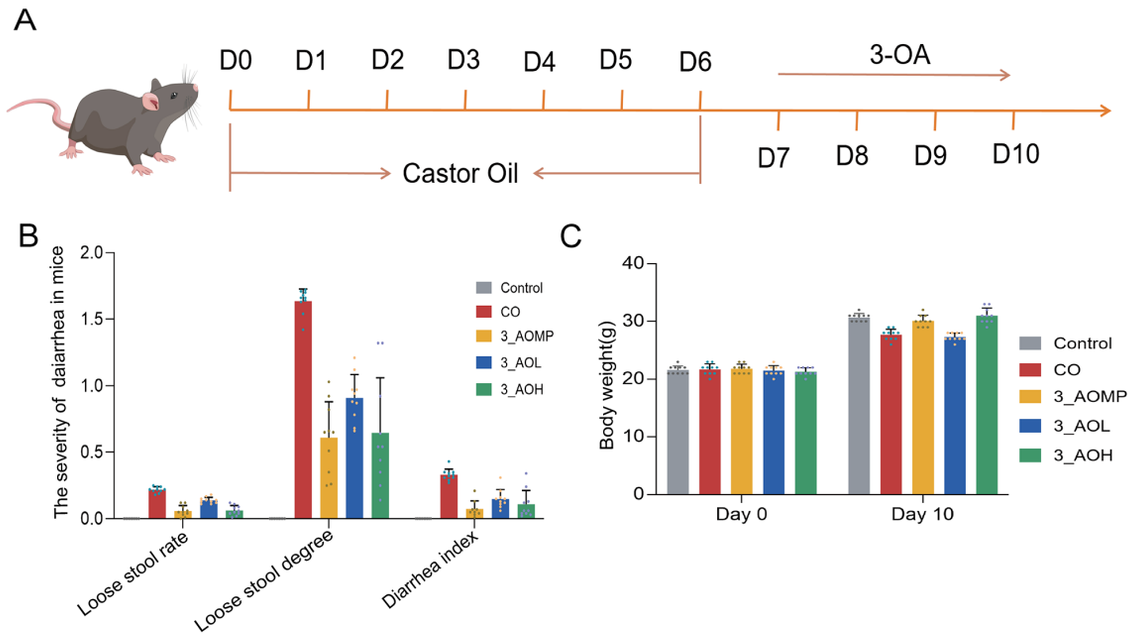



**Figure 8 Effects of 3-oxooctadecanoic acid on mouse gut health**

A: Timeline of mouse intestinal flora modeling experiment. B: Effects of different treatments on diarrhea severity in mice. Chart compares diarrhea severity among mice in different treatment groups using three indicators: loose stool rate, loose stool degree, and diarrhea index. Groups include Control, CO, 3_AOMP, 3_AOL, and 3_AOH. C: Body weight changes in mice across treatment groups on days 0 and 10. Graph includes five treatment groups: Control, CO, 3_AOMP, 3_AOL, and 3_AOH.

remodeling.Differential metabolite analysis provided additional evidence that *HBB* deficiency reshaped the fecal metabolome. PCA separated *HBB* mutants from WT controls, and univariate analysis identified 177 up-regulated and 233 down-regulated metabolites in *HBB* mutants. These 410 differential metabolites provide crucial insights for further understanding the impact of *HBB* deficiency on the metabolome. Such changes may be linked to immune regulation, metabolic imbalance, and altered host-microbiota communication associated with *HBB* deficiency (Baker & Rutter, 2023; Su et al., 2022). Collectively, these findings identify fecal metabolites as potential indicators of *HBB* deficiency-associated intestinal disturbance and may be a basis for future biomarker discovery in β-thalassemia-related gastrointestinal dysfunction.

Microbiome profiling revealed significant differences in the gut microbiota between *HBB*-deficient and WT macaques across species, genus, and phylum levels. The most prominent shifts involved *Lactobacillus* and *Bacteroides*, suggesting that *HBB* deficiency may reshape intestinal microbial ecology. *Lactobacillus* is closely related to immune regulation (Charlet et al., 2020), and reduced *Lactobacillus* abundance may be associated with impaired immune tolerance or enhanced inflammatory responses (Bennett et al., 2020; Wilck et al., 2017). In contrast, *Bacteroides* is involved in diverse metabolic processes, and altered *Bacteroides* abundance may reflect long-term regulatory effects of gene editing on the gut microbiota (Charlet et al., 2020; Wexler, 2007). Consistent with this interpretation, Zhang et al. (2024a) reported that *Bacteroides uniformis* degrades β-glucan to promote *Lactobacillus johnsonii*, increase indole-3-lactic acid levels, and alleviate colitis. Thus, the reduced abundance of *Lactobacillus* species and altered *Bacteroides* enrichment observed in *HBB*-deficient macaques may affect immune regulation, microbial metabolic activity, and disease susceptibility (Chen et al., 2023; Gao et al., 2018). Species richness analysis further showed a significantly lower Chao1 index in *HBB* mutants than in WT macaques, suggesting that *HBB* deficiency may reduce gut microbial richness.These changes may also be accompanied by reduced microbial gene diversity in disease states associated with *HBB* deficiency (Liikonen et al., 2024). However, differences in microbial evenness and overall community diversity between groups were comparatively modest.

Functional analysis further indicated that *HBB* deficiency was associated with alterations in microbial pathways related to amino acid metabolism (Agus et al., 2018; Li et al., 2022), lipid metabolism (Brown et al., 2023; Schoeler & Caesar, 2019), and energy metabolism (Amabebe et al., 2020; Fan & Pedersen, 2021) in the *HBB* mutants. These alterations in metabolic pathways may reflect coordinated interactions among altered microbial composition, host metabolic demand, and *HBB* deficiency-associated physiological stress. Integrated enrichment analysis identified the “Tricarboxylic Acid Cycle (TCA Cycle)” as a prominent pathway associated with metabolic function and species distribution, with a high RichFactor and enrichment of oxoglutaric acid together with four differentially expressed genes (*porA*, *porB*, *korC*, and *oorC*). This finding supports an important role for TCA cycle-related microbial functions in metabolic regulation (Liu et al., 2023). CCA further showed that oxoglutaric acid was strongly correlated with multiple microbial species, indicating that this metabolite may play a central role in species distribution and metabolic functions. These findings provide a mechanistic basis for understanding how *HBB* deficiency may alter microbiota-associated metabolic networks (Canzler & Hackermüller, 2020) and suggest that these pathways may serve as key bridges for interactions between gut microbiota and host physiology (Gomez-Eguilaz et al., 2019).

Integrated KEGG enrichment analysis showed strong

concordance between metabolomic and metagenomic datasets, with annotated metabolites and nonredundant microbial genes mapping to amino acid metabolism, lipid metabolism, secondary metabolite biosynthesis, cofactor and vitamin metabolism, xenobiotic biodegradation and metabolism, and carbohydrate metabolism. Metabolomic analysis indicated that phenylalanine metabolism exhibited an overall up-regulation trend in *HBB* mutants. In contrast, metagenomic analysis indicated that genes related to phenylalanine biosynthesis were significantly enriched in the WT group, but not in the *HBB* mutants. This discordance suggests an imbalance between microbial phenylalanine biosynthesis and host or microbial phenylalanine metabolism in *HBB* mutants and may represent an early pathological marker of β-thalassemia-associated *HBB* mutation. Consistent with this interpretation, elevated phenylalanine oxidation products, including o-tyrosine and m-tyrosine, have been reported in patients with β-thalassemia and proposed as biomarkers of protein oxidative damage in moderate disease (Matayatsuk et al., 2007). Therefore, phenylalanine metabolic dysregulation may be closely linked to oxidative stress and broader pathophysiological processes in β-thalassemia.

The *HBB*-mutant cynomolgus macaque model demonstrated strong concordance with human β-thalassemia. At the phylum level, *HBB*-mutant macaques exhibited an increased Proteobacteria/Firmicutes ratio and a relative decrease in *Bacteroidetes*. At the genus and species levels, *Lactobacillus*, particularly *L. johnsonii* and *L. amylovorus*, was significantly reduced, whereas *Bacteroides* was enriched. These features resemble human stool profiles characterized by loss of short-chain fatty acid-producing bacteria and expansion of potentially pathogenic taxa. Metabolomic changes further included decreased short-chain fatty acids, including butyrate and propionate, and increased primary bile acids, including glycocholic acid and taurocholic acid (HMDB0082176), consistent with published human data. Collectively, these microbiome-metabolite-host phenotypic parallels establish the model as a relevant non-human primate platform for mechanistic and interventional studies of the blood-gut axis in β-thalassemia (Djulejic et al., 2024; Nonejuie et al., 2024).

Recent non-human primate studies have also revealed disease-specific microbiota-host signatures, suggesting that distinct pathological states may carry discriminable microbial and metabolic fingerprints. In rhesus macaques challenged with *Mycobacterium tuberculosis* strains of varying virulence, global gut-community shifts were modest; however, baseline microbiota profiles before infection predicted subsequent disease severity. Susceptible animals showed enrichment of Lachnospiraceae and Clostridiaceae, and depletion of Streptococcaceae. After infection, Erysipelotrichaceae declined and Ruminococcaceae expanded, a pattern consistently reproduced across three independent experiments using distinct *M. tuberculosis* strains (Yang et al., 2022). Fecal metagenomic analysis in Parkinson's disease (PD) models has similarly identified gut dysbiosis, characterized by reduced α-diversity and altered symbiotic taxa, particularly *Streptococcus*, *Butyrivibrio*, and *Clostridium* species, with disease-associated microbial changes correlating with metabolites such as sphingomyelins and phospholipids (Gao et al., 2024). In a cynomolgus monkey stroke model, fecal microbiota transplantation has revealed links between post-stroke sleep disruption and decreased cerebrospinal fluid levels of probiotic-associated markers, including *Lactobacillus*, GABA, and glutamine (Liang et al., 2024). These findings collectively underscore the importance of non-human primate models for studying gut dysbiosis (Liang et al., 2024).

Cardiovascular complications remain a major clinical burden in thalassemia and are closely linked to endothelial dysfunction (Chuljerm et al., 2025). Circulating endothelial biomarkers, including intercellular adhesion molecule-1 (ICAM-1), vascular cell adhesion molecule-1 (VCAM-1), E-selectin, and P-selectin, have been used to evaluate vascular injury and cardiovascular risk in this population. Plasma endothelin-1 (ET-1) dynamics during transfusion have also been examined in thalassemic patients, supporting the value of vascular biomarkers for monitoring disease-associated clinical states (Viprakasit et al., 2002). In hemoglobin E/β-thalassemia, reduced nitrite reductase activity of deoxyhemoglobin correlates with platelet activation, further indicating that specific metabolites may serve as biomarkers (Chamchoi et al., 2018). In the present study, functional validation in a castor oil-induced diarrhea mouse model showed that high-dose 3-oxooctadecanoic acid (HMDB0254633; 3_AOH) attenuated diarrhea, as reflected by reduced loose stool rate, stool consistency grade, and diarrhea index, together with partial recovery of body weight (Zhu et al., 2022). The 3_AOH group also showed improvement in gut microbiota composition, suggesting that microbiota modulation may contribute to the antidiarrheal effect (Guo et al., 2022). These findings indicate that 3-oxooctadecanoic acid may reduce intestinal dysfunction by restoring microbial balance and supporting gut barrier integrity, although the underlying mechanism requires further experimental validation.

Non-human primates, including cynomolgus monkeys, share closer genetic, physiological, immunological, and metabolic similarity to humans than rodents, making them valuable models for complex human diseases such as β-thalassemia. Primate-specific developmental features, including the extended timing of neurogenesis relative to rodents, illustrate the importance of primate models for capturing human-relevant biological processes (De Sousa et al., 2015; Smith & French, 1997). Although rodent studies have provided important mechanistic insights, species-level differences in physiology, immune regulation, metabolism, and intestinal ecology can limit direct extrapolation to human disease. The use of *HBB*-mutant cynomolgus macaques therefore helps bridge this translational gap by providing a model that more closely approximates human β-thalassemia-associated host-microbiota interactions(Miller et al., 2016). The blood-gut axis involves coordinated interactions among host genetics, gut microbiota, and metabolic pathways, and non-human primates provide a biologically relevant model for studying these interactions. Evidence that primate cortical neural precursors exhibit an extended postmitotic phase of fate plasticity underscores the capacity of primate models to reveal biological processes that are not fully captured in rodents (Zhu et al., 2020).

The current study has several limitations. The relatively small sample size may reduce statistical power and limit the ability to capture interindividual variation in gut microbiota and metabolite profiles. This study included eight cynomolgus monkeys, comprising three WT and five *HBB* mutants. Although this cohort enabled detection of genotype-associated

differences in microbial composition and fecal metabolites, larger populations are needed to validate differential microbial taxa, metabolic features, and pathway-level associations. This limitation is particularly relevant for high-dimensional metagenomic and metabolomic analyses, in which effect size estimates can be influenced by sample size. Future studies with expanded non-human primate cohorts, independent validation datasets, and collaborative data integration will be important for confirming these findings and refining the mechanistic framework of the blood-gut axis in β-thalassemia. Such efforts will strengthen biological inference and improve the translational value of *HBB*-mutant cynomolgus macaques for mechanistic and interventional research.

## CONCLUSION

This study provides a framework for understanding how *HBB* deficiency reshapes host metabolic function through gut microbiota-associated pathways. Integrated metabolomic analysis revealed marked differences between *HBB* mutants and WT controls, particularly in amino acid and lipid metabolism. Metagenomic profiling further showed significant differences in the abundances of *Lactobacillus* and *Bacteroides*, accompanied by reduced microbial diversity in *HBB* mutants. Functional analysis indicated that *HBB* deficiency significantly disrupted key metabolic pathways, including amino acid and energy metabolism. In a castor oil-induced diarrhea model in C57BL/6 mice, high-dose 3-oxooctadecanoic acid alleviated diarrhea and improved gut microbiota composition, supporting its potential relevance as a functional metabolite associated with intestinal homeostasis. However, further studies are needed to determine how gut microbiota alterations directly contribute to the pathogenesis of *HBB*-related disorders, including β-thalassemia and sickle cell anemia, and whether microbial metabolites modulate disease phenotypes through immune regulation, iron metabolism, and host metabolic signaling.

## DATA AVAILABILITY

The raw sequence data reported in this paper have been deposited in the Science Data Bank (DOI: 10.57760/sciencedb.j00139.00288), NCBI database (BioProjectID PRJNA1458028), and Genome Sequence Archive (GSA) at the National Genomics Data Center, China National Center for Bioinformation / Beijing Institute of Genomics, Chinese Academy of Sciences (accession number: CRA029468).

## SUPPLEMENTARY DATA

Supplementary data to this article can be found online.

## COMPETING INTERESTS

The authors declare that they have no competing interests.

## AUTHORS' CONTRIBUTIONS

B.Z.L., X.Y.Z., and Z.W.S. conducted comprehensive data analysis, interpreted the results, and prepared the first draft of the manuscript. J.W. and J.T.Z. assisted in data analysis, validated data accuracy, and contributed to data visualization. Y.H. and K.Q.C. were responsible for collecting and initially processing the samples. J.G.Z. and S.H.Y. reviewed and edited the manuscript, suggesting substantial revisions to improve clarity and coherence. J.L.Y. designed the research framework, secured funding, supervised the entire project, and ensured coordination among all team members. All authors read and approved the final version of the manuscript.

## ACKNOWLEDGMENTS

We would like to thank all members of our laboratory.

## REFERENCES

Agus A, Planchais J, Sokol H. 2018. Gut microbiota regulation of tryptophan metabolism in health and disease. *Cell Host & Microbe*, **23**(6): 716–724.

Amabebe E, Robert FO, Agbalalah T, et al. 2020. Microbial dysbiosis-induced obesity: Role of gut microbiota in homoeostasis of energy metabolism. *British Journal of Nutrition*, **123**(10): 1127–1137.

Baker SA & Rutter J. 2023. Metabolites as signalling molecules. *Nature Reviews Molecular Cell Biology*, **24**(5): 355–374.

Bennett PR, Brown RG, Macintyre DA. 2020. Vaginal microbiome in preterm rupture of membranes. *Obstetrics and Gynecology Clinics of North America*, **47**(4): 503–521.

Brown EM, Clardy J, Xavier RJ. 2023. Gut microbiome lipid metabolism and its impact on host physiology. *Cell Host & Microbe*, **31**(2): 173–186.

Canzler S, Hackermüller J. 2020. multiGSEA: A GSEA-based pathway enrichment analysis for multi-omics data. *BMC Bioinformatics*, **21**(1): 561.

Chamchoi A, Srihirun S, Paiboonsukwong K, et al. 2018. Decreased nitrite reductase activity of deoxyhemoglobin correlates with platelet activation in hemoglobin E/ß-thalassemia subjects. *PLoS One*, **13**(9): e0203955.

Charlet R, Bortolus C, Sendid B, et al. 2020. *Bacteroides thetaiotaomicron* and *Lactobacillus johnsonii* modulate intestinal inflammation and eliminate fungi via enzymatic hydrolysis of the fungal cell wall. *Scientific Reports*, **10**(1): 11510.

Chen TT, Chen X, Zhang SS, et al. 2021. The genome sequence archive family: Toward explosive data growth and diverse data types. *Genomics, Proteomics & Bioinformatics*, **19**(4): 578–583.

Chen X, Wu R, Li L, et al. 2023. Pregnancy-induced changes to the gut microbiota drive macrophage pyroptosis and exacerbate septic inflammation. *Immunity*, **56**(2): 336–352. e9.

Chuljerm H, Maneekesorn S, Thorup G, et al. 2025. The relevance of endothelial dysfunction biomarkers in thalassemia patients and healthy individuals: A systematic review and meta-analysis. *International Journal of Molecular Sciences*, **26**(8): 3842.

De Sousa MBC, de Menezes Galvão AC, Sales CJR, et al. 2015. Endocrine and cognitive adaptations to cope with stress in immature common marmosets (*Callithrix jacchus*): Sex and age matter. *Frontiers in Psychiatry*, **6**: 160.

Djulejic V, Ivanovski A, Cirovic A, et al. 2024. Increased cadmium load, vitamin d deficiency, and elevated FGF23 levels as pathophysiological factors potentially linked to the onset of acute lymphoblastic leukemia: A review. *Journal of Personalized Medicine*, **14**(10): 1036.

Ebeling M, Küng E, See A, et al. 2011. Genome-based analysis of the nonhuman primate *Macaca fascicularis* as a model for drug safety assessment. *Genome Research*, **21**(10): 1746–1756.

Fan Y, Pedersen O. 2021. Gut microbiota in human metabolic health and disease. *Nature Reviews Microbiology*, **19**(1): 55–71.

Frąckowiak J, Komorowicz I, Sajnóg A, et al. 2025. Do probiotics and iron supplementation have any impact on element distribution in rat kidneys? - bioimaging by laser ablation inductively coupled plasma mass spectrometry. *Talanta*, **283**: 127112.

Galié S, García-Gavilán J, Camacho-Barcía L, et al. 2021. Effects of the mediterranean diet or nut consumption on gut microbiota composition and fecal metabolites and their relationship with cardiometabolic risk factors. *Molecular Nutrition & Food Research*, **65**(19): 2000982.

Gao J, Xu K, Liu HN, et al. 2018. Impact of the gut microbiota on intestinal immunity mediated by tryptophan metabolism. *Frontiers in Cellular and Infection Microbiology*, **8**: 13.

Gao JM, Xia SY, Hide G, et al. 2024. Multiomics of parkinsonism cynomolgus monkeys highlights significance of metabolites in interaction between host and microbiota. *npj Biofilms and Microbiomes*, **10**(1): 61.

Glenn JD & Mowry EM. 2016. Emerging concepts on the gut microbiome

and multiple sclerosis. *Journal of Interferon & Cytokine Research*, **36**(6): 347–357.

Gomez-Eguilaz M, Ramon-Trapero JL, Perez-Martinez L, et al. 2019. The microbiota-gut-brain axis and its great projections. *Revista de Neurología*, **68**(3): 111–117.

Groussin M, Mazel F, Sanders JG, et al. 2017. Unraveling the processes shaping mammalian gut microbiomes over evolutionary time. *Nature Communications*, **8**(1): 14319.

Gu K, Wu AM, Yu B, et al. 2023. Iron overload induces colitis by modulating ferroptosis and interfering gut microbiota in mice. *Science of the Total Environment*, **905**: 167043.

Guo XH, Okpara ES, Hu WT, et al. 2022. Interactive relationships between intestinal flora and bile acids. *International Journal of Molecular Sciences*, **23**(15): 8343.

He PD, Yu LL, Tian FW, et al. 2022. Dietary patterns and gut microbiota: The crucial actors in inflammatory bowel disease. *Advances in Nutrition*, **13**(5): 1628–1651.

Heintz-Buschart A, Wilmes P. 2018. Human gut microbiome: Function matters. *Trends in Microbiology*, **26**(7): 563–574.

Huang Y, Ding CH, Liang PP, et al. 2019. *HBB*-deficient *Macaca fascicularis* monkey presents with human β-thalassemi. *Protein & Cell*, **10**(7): 538–542.

Hugenholtz F, De Vos WM. 2018. Mouse models for human intestinal microbiota research: A critical evaluation. *Cellular and Molecular Life Sciences*, **75**(1): 149–160.

Lertsuwan K, Wongdee K, Teerapornpuntakit J, et al. 2018. Intestinal calcium transport and its regulation in thalassemia: Interaction between calcium and iron metabolism. *The Journal of Physiological Sciences*, **68**(3): 221–232.

Li MX, Li MY, Lei JX, et al. 2022. Huangqin decoction ameliorates DSS-induced ulcerative colitis: Role of gut microbiota and amino acid metabolism, mTOR pathway and intestinal epithelial barrier. *Phytomedicine*, **100**: 154052.

Liang JH, Xiong ZY, Lei QF, et al. 2024. Sleep dysfunction and gut dysbiosis related amino acids metabolism disorders in cynomolgus monkeys after middle cerebral artery occlusion. *ExPerimental Neurology*, **382**: 114970.

Liikonen V, Gomez-Gallego C, Kolehmainen M. 2024. The effects of whole grain cereals on tryptophan metabolism and intestinal barrier function: Underlying factors of health impact. *Proceedings of the Nutrition Society*, **83**(1): 42–54.

Liu H, Chen W, Tan SW, et al. 2023. An examination of the carbon metabolic pathways in Acinetobacter sp. TAC-1 in the context of poly (3-hydroxybutyrate-co-3-hydroxyvalerate) utilization. *Chinese Journal of Biotechnology*, **39**(11): 4663–4681. (in Chinese)

Malesza IJ, Bartkowiak-Wieczorek J, Winkler-Galicki J, et al. 2022. The dark side of iron: the relationship between iron, inflammation and gut microbiota in selected diseases associated with iron deficiency anaemia—a narrative review. *Nutrients*, **14**(17): 3478.

Manolis AA, Manolis TA, Melita H, et al. 2022. Gut microbiota and cardiovascular disease: Symbiosis versus dysbiosis. *Current Medicinal Chemistry*, **29**(23): 4050–4077.

Matayatsuk C, Poljak A, Bustamante S, et al. 2007. Quantitative determination of *ortho*- and *meta*-tyrosine as biomarkers of protein oxidative damage in β-thalassemia. *Redox Report*, **12**(5): 219–228.

Micheletti RG, Chiesa-Fuxench Z, Noe MH, et al. 2018. Stevens-Johnson syndrome/toxic epidermal necrolysis: A multicenter retrospective study of 377 adult patients from the United States. *Journal of Investigative Dermatology*, **138**(11): 2315–2321.

Miller CT, Freiwald WA, Leopold DA, et al. 2016. Marmosets: A neuroscientific model of human social behavior. *Neuron*, **90**(2): 219–233.

Nicholson JK, Holmes E, Kinross J, et al. 2012. Host-gut microbiota metabolic interactions. *Science*, **336**(6086): 1262–1267.

Nonejuie P, Wilantho A, McDonald D, et al. 2024. Differential gut microbiota composition in β-Thalassemia patients and its correlation with iron overload. *Scientific Reports*, **14**(1): 23858.

Schoeler M, Caesar R. 2019. Dietary lipids, gut microbiota and lipid metabolism. *Reviews in Endocrine and Metabolic Disorders*, **20**(4): 461–472.

Shalon D, Culver RN, Grembi JA, et al. 2023. Profiling the human intestinal environment under physiological conditions. *Nature*, **617**(7961): 581–591.

Smith TE, French JA. 1997. Psychosocial stress and urinary cortisol excretion in marmoset monkeys. *Physiology & Behavior*, **62**(2): 225–232.

Su XM, Gao YH, Yang RC. 2022. Gut microbiota-derived tryptophan metabolites maintain gut and systemic homeostasis. *Cells*, **11**(15): 2296.

Sun ZW, Wang J, Sun RP, et al. 2025. Bidirectional regulation of the brain-gut axis in *Macaca mulatta*: implications for wildlife conservation and experimentation. *Microbiology Spectrum*, **13**(9): e0133825.

Thursby E, Juge N. 2017. Introduction to the human gut microbiota. *Biochemical Journal*, **474**(11): 1823–1836.

Trompette A, Gollwitzer ES, Yadava K, et al. 2014. Gut microbiota metabolism of dietary fiber influences allergic airway disease and hematopoiesis. *Nature Medicine*, **20**(2): 159–166.

Turnbaugh PJ, Ley RE, Mahowald MA, et al. 2006. An obesity-associated gut microbiome with increased capacity for energy harvest. *Nature*, **444**(7122): 1027–1031.

Ul Ain N, Naveed M, Aziz T, et al. 2024. Mix-match synthesis of nanosynbiotics from probiotics and prebiotics to counter gut dysbiosis via AI integrated formulation profiling. *Scientific Reports*, **14**(1): 18397.

Viprakasit V, Kankirawatana S, Akarasereenont P, et al. 2002. Baseline levels of plasma endothelin-1 (ET-1) and changes during transfusion in thalassemic patients. *American Journal of Hematology*, **70**(3): 260–262.

Wang ZN, Klipfell E, Bennett BJ, et al. 2011. Gut flora metabolism of phosphatidylcholine promotes cardiovascular disease. *Nature*, **472**(7341): 57–63.

Wexler HM. 2007. *Bacteroides*: The good, the bad, and the nitty-gritty. *Clinical Microbiology Reviews*, **20**(4): 593–621.

Wilck N, Matus MG, Kearney SM, et al. 2017. Salt-responsive gut commensal modulates $T_H17$ axis and disease. *Nature*, **551**(7682): 585–589.

Yadegar A, Bar-Yoseph H, Monaghan TM, et al. 2024. Fecal microbiota transplantation: Current challenges and future landscapes. *Clinical Microbiology Reviews*, **37**(2): E0006022.

Yang F, Yang Y, Chen LM, et al. 2022. The gut microbiota mediates protective immunity against tuberculosis *via* modulation of lncRNA. *Gut Microbes*, **14**(1): 2029997.

Yuan JL, Sun ZW, Sun RP, et al. 2025. A spatiotemporal atlas of the gut microbiota in *Macaca mulatta brevicaudus*: Implications for health and environment. *Biology*, **14**(8): 980.

Zhang SS, Nie QX, Sun YG, et al. 2024a. *Bacteroides uniformis* degrades *β*-glucan to promote *Lactobacillus johnsonii* improving indole-3-lactic acid levels in alleviating colitis. *Microbiome*, **12**(1): 177.

Zhang WH, Zhuang JH, Guo YY, et al. 2024b. Pancreatic agenesis and altered m6A methylation in the pancreas of PDX1-mutant cynomolgus macaques. *Zoological Research*, **45**(6): 1188–1200.

Zhu J, Yu LQ, Fan Y, et al. 2022. *Camelina sativa* oil treatment alleviates castor oil-induced diarrhea in ICR mice by regulating intestinal flora composition. *Evidence-Based Complementary and Alternative Medicine*, **2022**: 5394514.

Zhu LF, Clayton JB, Van Haute MJS, et al. 2020. Sex bias in gut microbiome transmission in newly paired marmosets (*Callithrix jacchus*). *mSystems*, **5**(2): e00910.

Zhu WF, Gregory JC, Org E, et al. 2016. Gut microbial metabolite TMAO enhances platelet hyperreactivity and thrombosis risk. *Cell*, **165**(1): 111–124.